CMS Physics Analysis Summary

Contact: cms-pag-conveners-top@cern.ch 2022/03/18

Measurement of the cross section of top quark-antiquark pair production in association with a W boson in proton-proton collisions at $\sqrt{s} = 13\,\text{TeV}$

The CMS Collaboration

Abstract

The cross section for the production of a top quark-antiquark pair in association with a W boson in proton-proton collisions at a center-of-mass energy of 13 TeV is measured in a data sample recorded by the CMS experiment that corresponds to an integrated luminosity of $138\,\text{fb}^{-1}$. Events with two or three leptons, electrons or muons, and additional jets are selected. A cross section of $868 \pm 40\,(\text{stat})^{+52}_{-50}\,(\text{syst})$ fb is measured. The production cross sections of a top quark pair with a W^+ and a W^- boson are measured as $553^{+30}_{-29}\,(\text{stat})^{+31}_{-30}\,(\text{syst})$ fb and $343 \pm 26\,(\text{stat}) \pm 25\,(\text{syst})$ fb, respectively, and the corresponding ratio of the two cross sections is $1.61^{+0.15}_{-0.14}\,(\text{stat})^{+0.07}_{-0.05}\,(\text{syst})$. The measured cross sections for the studied processes are in agreement with standard model predictions within two standard deviations.

1 Introduction

The production of top quark-antiquark pairs with vector bosons ($t\bar{t}V$) is sensitive to the electroweak (EW) couplings of the top quark. The $t\bar{t}V$ processes of the weak interaction between a top quark and a W or a Z boson provide a direct measurement of the weak couplings of the top quark. These processes can receive sizable contributions from phenomena beyond the SM (BSM) [1–3]. Events in which top quarks are produced in association with a W boson ($t\bar{t}W$) are rather different from the $t\bar{t}V$ processes that involve neutral vector bosons: a W boson cannot be radiated from the final-state top quarks in the $t\bar{t}W$ process, and the dominant contribution to the production in this case is associated with quark-antiquark and (anti)quark-gluon initial states. Representative Feynman diagrams for the $t\bar{t}W$ process at leading (LO) and next-to-leading order (NLO) in quantum chromodynamics (QCD) and EW couplings are shown in Fig. 1.

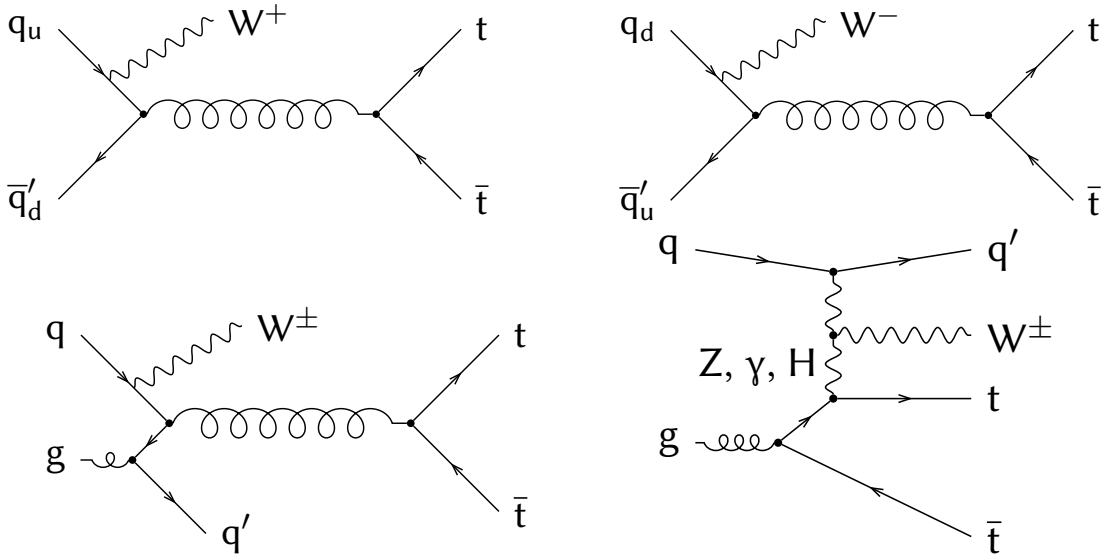

Figure 1: Representative Feynman diagrams that contribute to the $t\bar{t}W$ production at LO (top) and NLO (bottom), where "q_u" and "q_d" refer to up- and down-type quarks, respectively.

The absence of gluon-gluon initial states in $t\bar{t}W$ production leads to a sizable difference between production rates for the $t\bar{t}W^+$ and $t\bar{t}W^-$ processes because of the interference between valence- and sea-quark parton density functions (PDFs). At the level of final-state particles, the charge asymmetry is further enhanced because of the presence of spin correlations [4]. Compared to other $t\bar{t}V$ processes, the $t\bar{t}W$ process receives large corrections from the EW production diagrams at NLO, representing an important challenge for calculation of theoretical uncertainties in this process.

The cross section for $t\bar{t}W$ production was previously measured in pp collisions at a center-of-mass energy $\sqrt{s} = 13\,\text{TeV}$ by the CMS [5] and ATLAS [6] Collaborations, using $36\,\text{fb}^{-1}$ of integrated luminosity. In recent experimental studies of $t\bar{t}$ production in association with a Higgs boson ($t\bar{t}H$) [7, 8] and the production of four top quarks ($t\bar{t}t\bar{t}$) [9, 10], a tension was observed between the measured and predicted production cross sections for the $t\bar{t}W$ process, which represents one of the dominant backgrounds in these studies. It has been shown that the observed difference can be attributed to missing NLO corrections in theoretical calculations for this process [11–16].

This note presents a measurement of the inclusive $t\bar{t}W$ production cross section, which is per-

formed in final states with two or three charged leptons (electrons or muons). In dileptonic events, both leptons are required to have the same charge. The dominant background contributions are associated with the presence of "nonprompt" leptons originating from hadron decays, as well as misidentified leptons from jets or hadrons. Suppression of these background events relies on multivariate analysis (MVA) techniques, which are optimized to distinguish between the prompt leptons originating from W boson decays and the nonprompt leptons. Additional background contributions in final states involving electrons are associated with misreconstruction of electron charge and production of electrons from internally-converted photons. Background contributions also include the $t\bar{t}Z$ and $t\bar{t}H$ processes, as well as an associated production of a W and a Z boson (WZ), and three W bosons. Additional sources of background events involve processes with an associated production of pairs of top quarks and vector bosons ($t\bar{t}VV$).

The note is organized as follows: In Section 2 the data set and simulated samples are described. In Sections 3 and 4 the object and event selections are defined, respectively. Analysis strategy is discussed in Section 5 followed by description of estimation of background processes in Section 6. The main sources of experimental and theoretical systematic uncertainties are presented in Section 7. Finally, the results and a summary are given in Sections 8 and 9, respectively.

2 Data and simulated samples

The present study uses pp collision data recorded at $\sqrt{s} = 13\,\text{TeV}$ with a total integrated luminosity of $138\,\text{fb}^{-1}$. The collected data correspond to the data-taking periods in 2016–2018. Events are required to pass selection criteria defined at trigger level that include the presence of one, two, or three reconstructed leptons [17].

The Monte Carlo (MC) simulated samples for the $t\bar{t}W$ signal and background processes are used to estimate expected number of events, train multivariate classifiers, and assess systematic uncertainties. Simulated events for the $t\bar{t}W$ process are generated at the NLO accuracy in QCD using the MADGRAPH5_aMC@NLO 2.6.0 [18] program. At NLO precision, any observable that is associated with the $t\bar{t}W$ process is sensitive to terms of the order of $\alpha_s\alpha^3$ and $\alpha_s^3\alpha$ [19], where α_s is the strong coupling constant and α is the fine-structure constant. The $\alpha_s^3\alpha$ term is included in NLO QCD computations while the $\alpha_s\alpha^3$ term is simulated with MADGRAPH5_aMC@NLO [2, 15] and included in the analysis. The cross section that is used to normalize the $t\bar{t}W$ prediction is $592^{+155}_{-96}(\text{scale})^{+12}_{-12}(\text{PDF})$ fb and is computed up to the next-to-next-to-leading logatihmic (NNLL) accuracy, matched to the complete NLO results including QCD and EW effects [12]. Two alternative simulated samples are generated at NLO accuracy with MADGRAPH5_aMC@NLO for the $t\bar{t}W$ process in order to study systematic uncertainties associated with the choice of a color-reconnection model [20].

The MADGRAPH5_aMC@NLO generator is used to simulate events at NLO accuracy for background processes, including the production of $t\bar{t}$ or a single top quark in association with a vector boson ($t\bar{t}\gamma$, $t\bar{t}Z$, tZq, and $t\gamma$), the $t\bar{t}t\bar{t}$, Drell-Yan, VVV and WZ processes, as well as production of a vector boson in association with a Higgs boson (VH). Background processes with production of a top quark in association with a Higgs boson (tHq and tHW), as well as the $t\bar{t}VV$ process, are generated at LO accuracy using the MADGRAPH5_aMC@NLO generator. The POWHEG2 [21–23] program is used to generate samples with the production of two W bosons (WW), gluon-gluon-initiated ZZ production, ZZ production via vector boson fusion, $t\bar{t}$, and $t\bar{t}H$ production. Multijet events are generated with PYTHIA 8.226 (8.230) [24] in 2016 (2017–2018) samples and used in validation of background predictions associated with

processes involving nonprompt leptons.

The generated events are processed with the PYTHIA parton shower simulation. In simulated samples used to analyze data that were recorded in 2017–2018, the CP5 tuning parameters are used for the modelling of the underlying event [25, 26]. In the analysis of 2016 data the same set of parameters is used, where available. Samples are otherwise simulated with the CUETP8M1 [27] or CUETP8M2T4 [28] tunes. In event generation using MADGRAPH5_aMC@NLO, the FxFx merging scheme [29] is used for NLO samples and the MLM scheme for LO samples, in order to avoid possible double-counting effects between the matrix-element and parton-shower calculations. In generation of the aforementioned samples, the NNPDF3.1 [30] next-to-next-to-leading order (NNLO) PDFs are used.

Propagation of generated particles through the CMS detector and modelling of the detector response are performed using GEANT4 [31], assuming realistic alignment and calibration extracted from calibration and collision data. The simulated samples include minimum-bias pp interactions in the same or nearby bunch crossing (pileup), assuming a value of 69.2 mb for the total inelastic pp cross section.

3 Event reconstruction

The particle-flow (PF) algorithm [32] aims to reconstruct and identify each individual particle in an event to build τ leptons, jets, missing transverse momentum, and other physics objects [33–35]. The energy of photons is obtained from the ECAL measurement. The energy of electrons is determined from a combination of the electron momentum at the primary interaction vertex as determined by the tracker, the energy of the corresponding ECAL cluster, and the energy sum of all bremsstrahlung photons spatially compatible with originating from the electron track. The energy of muons is obtained from the curvature of the corresponding track. The energy of charged hadrons is determined from a combination of their momentum measured in the tracker and the matching ECAL and HCAL energy deposits, corrected for the response function of the calorimeters to hadronic showers. Finally, the energy of neutral hadrons is obtained from the corresponding corrected ECAL and HCAL energies.

The candidate vertex with the largest value of summed physics-object p_{T}^2 is taken to be the primary pp interaction vertex. The physics objects are the jets, clustered using the jet finding algorithm [36, 37] with the tracks assigned to candidate vertexes as inputs. The associated missing transverse momentum is taken as the negative vector sum of the p_{T} of those jets.

Electrons are identified with a multivariate discriminant [38] and are required to have $p_{\mathrm{T}} > 10\,\mathrm{GeV}$ and pseudorapidity $|\eta| < 2.5$. Electrons that are reconstructed within the region of $|\eta| > 1.479$ and $|\eta| < 1.566$ and those associated with tracks with more than one missing hit in the tracking system are excluded from the analysis.

Muons are identified as tracks in the central tracker consistent with either a track or several hits in the muon system, and associated with calorimeter deposits compatible with the muon hypothesis. Reconstructed muons must have $p_{\mathrm{T}} > 10\,\mathrm{GeV}$ and $|\eta| < 2.4$ and fulfill selection criteria on geometrical matching between the inner and the muon track, and on the quality of the global fit [39].

Lepton isolation uses information from the reconstruction at PF level. A "mini-isolation" variable is defined as sum of p_{T} of PF objects inside a cone $\Delta R = \sqrt{(\Delta\eta)^2 + (\Delta\phi)^2}$, excluding the lepton itself, where ΔR depends on p_{T} of the lepton (p_{T}^{ℓ}) as $\Delta R(p_{\mathrm{T}}^{\ell}) = 10/\min[\max(p_{\mathrm{T}}^{\ell}, 50), 200]$. The mini-isolation of a lepton divided by the lepton p_{T} must be smaller than 0.4. Electrons and

muons satisfying the aforementioned selection criteria are referred to as "loose" leptons in the following. Any loose electron is required to be at least $\Delta R = 0.05$ away from any loose muon.

The "tight" lepton selection criteria are defined to mainly suppress background events associated with the presence of nonprompt leptons. In addition to the loose criterion, the tight definition includes a selection requirement on an MVA discriminant "lepton MVA" [40–42] that corresponds to a prompt lepton selection efficiency of about 95% and a misidentification rate of nonprompt leptons of about 2%, as evaluated from MC simulations for leptons with $p_T > 25$ GeV. A tight electron must be not associated with a secondary vertex that is consistent with a photon conversion and must have a charge measurement consistent among three independent measurements [38]. The reconstructed energy of an electron in the HCAL must be less than 10% of the corresponding energy in the ECAL. Additionally, a criterion on the reconstructed electromagnetic shower width in units of the ECAL crystal spacing $\sigma_{\eta\eta}$ <0.011 (0.03) for the barrel (endcap), is used. The electron's energy must be compatible with the associated track momentum and expected energy loss ($1/E - 1/p > -0.04/\,\text{GeV}$). The impact parameters of a lepton track with respect to the primary interaction vertex, defined in the transverse (d_{xy}) and longitudinal (d_z) planes relative to the direction of colliding proton beams, must satisfy $|d_{xy}| < 0.05\,\text{cm}$ and $|d_z| < 0.1\,\text{cm}$, respectively. The impact parameter significance of the lepton track, defined as the absolute ratio between the impact parameter value calculated in 3D plane and its uncertainty, must be less than 8.

For each event, hadronic jets are clustered from the reconstructed particles using the anti-k_T algorithm [36, 37] with a distance parameter of 0.4. Jet momentum is determined as the vectorial sum of the momenta of all particles in the jet, and is found from simulation to be, on average, within 5 to 10% of the true momentum over the whole p_T spectrum and detector acceptance. Additional pp interactions within the same or nearby bunch crossings can contribute additional tracks and calorimetric energy depositions, increasing the apparent jet momentum. To mitigate this effect, tracks identified to be originating from pileup vertices are discarded and an offset correction is applied to correct for remaining contributions [43]. Jet energy corrections are derived from simulation studies so that the average measured energy of jets becomes identical to that of particle level jets. In situ measurements of the momentum balance in dijet, photon+jet, Z+jet, and multijet events are used to determine any residual differences between the jet energy scale in data and in simulation, and appropriate corrections are made [34]. Additional selection criteria are applied to each jet in order to remove jets potentially dominated by instrumental effects or reconstruction failures. Jets with $p_T > 25$ GeV and $|\eta| < 2.4$ are considered in the analysis, and those including a loose lepton among their PF constituents inside a cone of $\Delta R = 0.4$ are removed.

The DEEPJET algorithm [44–46] is used to identify b quark jets arising from hadronizaton of b hadrons (b-tagged jets). The "loose" and "medium" b tagging selection requirements used in this analysis correspond to b quark jet selection efficiencies of about 90% and 85% for jets with $p_T > 30\,\text{GeV}$ as estimated in simulated $t\bar{t}$ events. The corresponding misidentification rates of 10% and 1% for jets arising from u, d, s quarks or gluons, and 50% and 15% for jets originating from hadronization of c quarks are obtained in those events.

The missing transverse momentum vector $\vec{p}_T^{\,\text{miss}}$ is computed as a negative vector sum of p_T of all PF candidates in an event, and its magnitude is denoted as p_T^{miss} [35]. The $\vec{p}_T^{\,\text{miss}}$ is modified to account for corrections to the energy scale of reconstructed jets in event.

4 Event selection

Criteria used to select dileptonic and trileptonic events are made orthogonal by requiring the presence of exactly two or three loose leptons, respectively.

Exactly two tight leptons with electric charge of same sign are selected in the dileptonic channel with $p_{\mathrm{T}} > 30$ (25) GeV for the highest-p_{T} (leading) electron (muon). The second highest-p_{T} (subleading) lepton must have $p_{\mathrm{T}} > 20$ GeV. A reconstructed dilepton invariant mass must be larger than 30 GeV and, in case both leptons are electrons, not to be within 15 GeV of the Z boson mass. The two leptons must also be separated by $\Delta R > 0.4$. Events are selected with $p_{\mathrm{T}}^{\mathrm{miss}}$ of at least 30 GeV and are required to contain at least two jets, out of which at least two pass the loose b tagging selection, or at least one of the jets passes the medium b tagging selection.

In the trileptonic channel, events are selected with exactly three tight leptons with p_{T} of at least 25 GeV, 15 GeV, and 15 GeV for the leading, the subleading and the trailing lepton, respectively. The reconstructed invariant mass of each lepton pair must be larger than 12 GeV. In case the two leptons are of same flavor and of opposite sign, the reconstructed dileptonic invariant mass must not be within 10 GeV from the world-average Z boson mass [47]. The sum of charges of the three leptons is required to be ± 1 and events must contain at least two jets, among which at least one jet passes the medium b tagging selection.

5 Analysis strategy

A multiclassification neural network (NN) is used to distinguish the signal $\mathrm{t\bar{t}W}$ process and background events in the dileptonic channel. The NN has two hidden layers, with 128 and 64 nodes, respectively, and an output layer with four nodes: $\mathrm{t\bar{t}W}$, nonprompt leptons, $\mathrm{t\bar{t}Z}$ and $\mathrm{t\bar{t}H}$ used as a single category, and $\mathrm{t\bar{t}}\gamma$. An inclusive $\mathrm{t\bar{t}}$ sample is used to model the nonprompt lepton background, by selecting one tight and one loose lepton that must fail the tight requirement. The values of the $\mathrm{t\bar{t}W}$ output node of the NN are transformed to give an approximately linearly decreasing distribution for the total expected background, such that an equidistant binning results in a slowly varying signal-to-background ratio.

The input variables include several kinematic observables associated with the reconstructed leptons and jets, such as the transverse momenta, as well as azimuthal angle, ΔR and invariant masses calculated for lepton and lepton-jet combinations. The list of input variables also includes the b tagging probabilities of selected jets, in addition to the information about the flavor and charge of the leptons. Figure 2 compares the observed and predicted number of events in the distributions of the leading lepton p_{T}, leading jet p_{T}, jet and b tag multiplicities, and $p_{\mathrm{T}}^{\mathrm{miss}}$ variable.

The analysis strategy in the trileptonic channel relies on an event categorization based on the number of jets, b-tagged jets and the charges of selected leptons. A good agreement is observed between the number of observed and predicted events, as shown in Fig. 3. A common discriminant variable, based on the $m(3\ell)$ distribution, which shows a good discrimination between signal and background events, is used across the described event categories.

6 Background estimation

The nonprompt lepton background contributes to both the same-sign dileptonic and trileptonic signal regions. This background is estimated from data using a tight-to-loose ratio method [40,

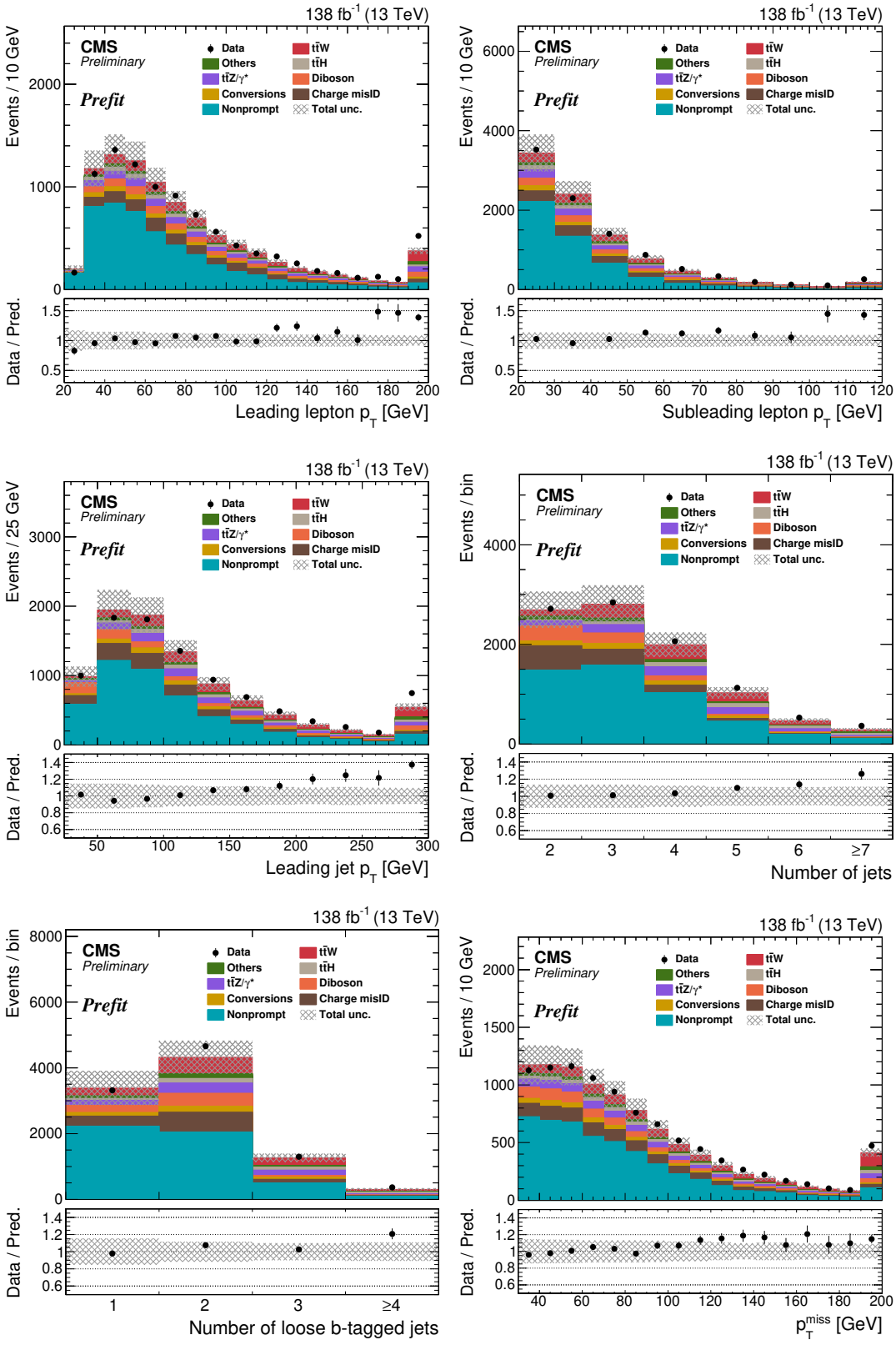

Figure 2: Comparison between the number of observed and predicted events for the leading (upper left) and the subleading (upper right) lepton p_T, the leading jet p_T (middle left), the total number of jets (middle right), the number of loose b-tagged jets (lower left), and p_T^{miss} (lower right) in same-sign dileptonic events. The lower panels of each plot show the ratio between the number of observed events in data and the total number of predicted events. The error bars show the statistical uncertainty in data, whereas the hatched bands represent the total systematic uncertainty. The last bins include the overflows.

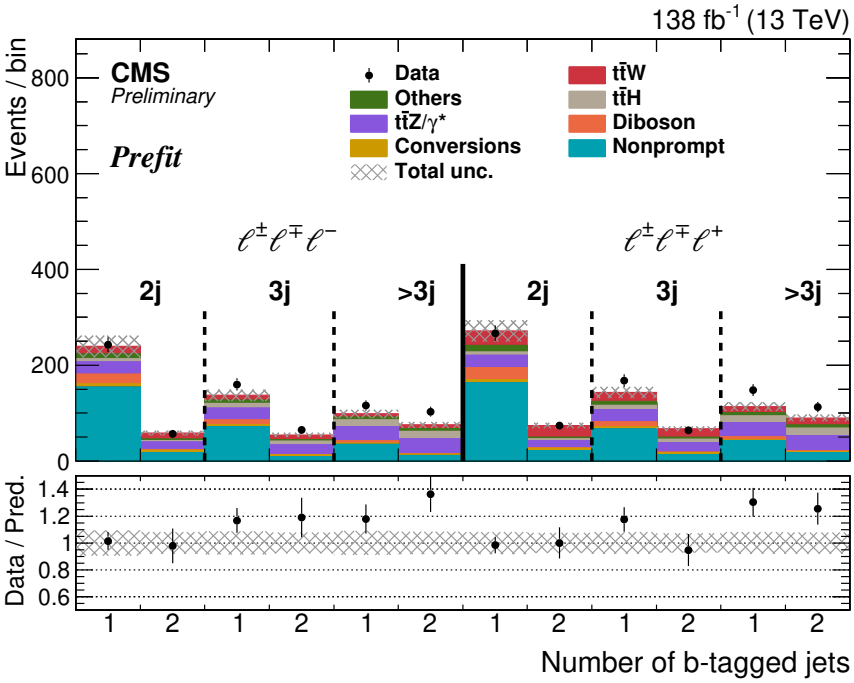

Figure 3: Comparison between the observed and predicted number of events in the trileptonic channel. Events with positive or negative sum of lepton charges are categorized by the number of jets j and b-tagged jets. The lower panels of each plot show the ratio between the number of observed events in data and the total number of predicted events. The error bars show the statistical uncertainty in data, whereas the hatched bands represent the total systematic uncertainty.

48]. The lepton misidentification rate is defined as the probability of a nonprompt lepton that passes the loose selection criteria to also satisfy the tight selection. This rate is measured in a kinematic region in data that is enriched in multijet events, and is parameterized as a function of the lepton p_T and $|\eta|$. The selection criteria include the presence of at least one tight lepton without applying the lepton MVA requirement. The selected leptons must be separated from any reconstructed jet in the event by at least $\Delta R = 0.7$. Any remaining contributions associated with the processes involving prompt leptons are subtracted using simulation. The number of multijet events is estimated from a maximum likelihood fit to the distribution of the variable defined as $m_T^{\text{fixed}} = \sqrt{2p_T^{\text{fixed}}|p_T^{\text{miss}}|(1-\cos(\Delta\phi))}$, where p_T^{fixed} is a constant value set to 35 GeV, and the symbol $\Delta\phi$ represents the angle in the transverse plane between the lepton momentum and p_T^{miss}. The m_T^{fixed} observable exploits the fact that the p_T^{miss} that is reconstructed in multijet events is mainly due to resolution effects and is typically small, resulting in a falling distribution in m_T^{fixed}, while the m_T^{fixed} distribution of events with the production of a W boson has a broad maximum around 80 GeV. Since the p_T^{fixed} is a fixed value, there is no dependence of m_T^{fixed} on the lepton p_T. The nonprompt lepton background is estimated by applying the measured misidentification rates in events with at least one loose lepton. This background is validated in a kinematic region with same-sign dilepton events including the requirement of $p_T^{\text{miss}} < 30$ GeV. Comparison between the number of events of estimated background and data is presented in Fig. 4. This validation region is used to assign an additional systematic uncertainty on the nonprompt lepton background prediction.

Background contributions arising from the mismeasured electron charge ("Charge MisID") are relevant in the same-sign dileptonic channel. As an electron passes through the detector, it can radiate a photon that may subsequently convert to an electron-positron pair, where either the electron or the positron gains most of the photon's energy. The charge misidentification rate is measured in Drell-Yan and $t\bar{t}$ simulated samples using tight electrons as a function of the lepton p_T and $|\eta|$. This rate is defined as probability that the reconstructed charge differs from its generated value. The measured misidentification rates are validated in an orthogonal kinematic region with two electrons of the same charge that have a reconstructed dileptonic invariant mass within 10 GeV of the Z boson mass. The predicted number of background events is estimated from data by applying the misidentification rates in events with two oppositely charged electrons. The charge misidentification rate for muons was found to be negligible.

Background processes with one or more reconstructed electrons due to the conversion of a photon ("Conversions") are estimated from simulation. In these events an electron or a positron typically carries most of the energy of the converted photon, while the other lepton is of low energy and not reconstructed.

Backgrounds that are mainly associated with the presence of prompt leptons are modeled using simulations, and are either normalized to the corresponding theoretical cross sections. These backgrounds arise from $t\bar{t}H$, $t\bar{t}Z/\gamma^*$, dibosons (WZ and ZZ) as well as the processes with smaller predicted cross sections, which collectively represent the "other" category (VVV, $t\bar{t}VV$, $t\bar{t}t\bar{t}$, tHq, tZq and other rare processes).

Predictions for the processes with diboson production, such as WZ and ZZ, as well as $t\bar{t}Z$ events are compared to data in dedicated kinematic control regions. A kinematic region in data that is enriched in WZ and $t\bar{t}Z$ events is defined by selecting trileptonic events with the presence of two same-flavor oppositely-charged leptons with an invariant mass within 10 GeV of the Z boson mass. Events are classified as a function of the number of jets and b-tagged jets, as shown in Fig. 5. Potential differences between the predicted number of events for these background processes and the data are studied as a function of the number of reconstructed

jets in the event. This control region is further split into four event categories based on the flavors of selected leptons.

The kinematic region enriched in ZZ events in data is defined by requiring exactly four leptons with p_T above 25, 15, 15, and 10 GeV, in the order of the largest lepton p_T, respectively, and at least one Z boson candidate, which is defined as an opposite-sign same-flavor lepton pair with an invariant mass within 10 GeV of the predicted Z boson mass. Events are classified in four bins as a function of the number of Z candidates, the number of jets, and the number of b-tagged jets. A comparison for the observed number of events and the prediction is shown in Fig. 6.

7 Systematic uncertainties

Multiple sources of systematic uncertainty may modify the signal and background event yields and the distributions of the discriminating observables used for the signal extraction. The main sources of experimental and theoretical systematic uncertainties are described below.

Luminosity The integrated luminosities for the 2016, 2017, and 2018 data-taking years have 1.2–2.5% individual uncertainties [49–51], while the overall uncertainty for the 2016–2018 period is 1.6%.

Pileup The distribution of the number of additional proton-proton interactions per event in simulation is matched to data by reweighting the profile of the true number of interactions to the one inferred from the instantaneous luminosity profile in data. A systematic uncertainty is estimated by varying the assumed minimum-bias cross section of 69.2 mb by $\pm$4.6%. This uncertainty is propagated throughout the analysis, and is considered fully correlated among the data-taking years.

Trigger efficiency Per-event weights that depend on the lepton p_T are applied to the simulated samples in order to correct for discrepancies in trigger efficiencies between data and simulation. The impact on the final discriminants due to the trigger efficiency uncertainty is estimated by varying these scale factors within their uncertainties, which are determined to be 2% overall. The uncertainty is treated as uncorrelated among data-taking years, as well as between the dileptonic and trileptonic channels. A separate uncertainty is defined in each lepton flavor category in the dilepton channel.

L1 Prefiring During the 2016 and 2017 data-taking, a gradual shift in the timing of the inputs of the ECAL L1 trigger in the region at $|\eta| > 2.0$ caused a specific trigger inefficiency. Correction factors were computed from data and applied to the acceptance evaluated by simulation, correlated between 2016 and 2017. As expected in analyses that do not rely on forward objects at the L1 trigger stage, the effect on the results is small (below 1%).

Lepton efficiency The efficiency of the tight lepton selection is measured in data and simulation using the tag-and-probe method in $Z \to \ell^+\ell^-$. Per-lepton corrections are derived, and the systematic uncertainty is obtained and found to be at most a few percent in each bin. It is assumed to be uncorrelated among lepton flavors, as well as data-taking years.

Jet energy scale and resolution The variations of the jet momenta due to the uncertainty on the jet energy scale and resolution are taken into account as 21 uncertainty sources corresponding to different detector regions, taking into account the year-to-year correlations. Uncertainties in the p_T^{miss} resolution and response are accounted for by varying the jet energy scale in simulation within their respective uncertainties and recomputing the missing transverse momentum after

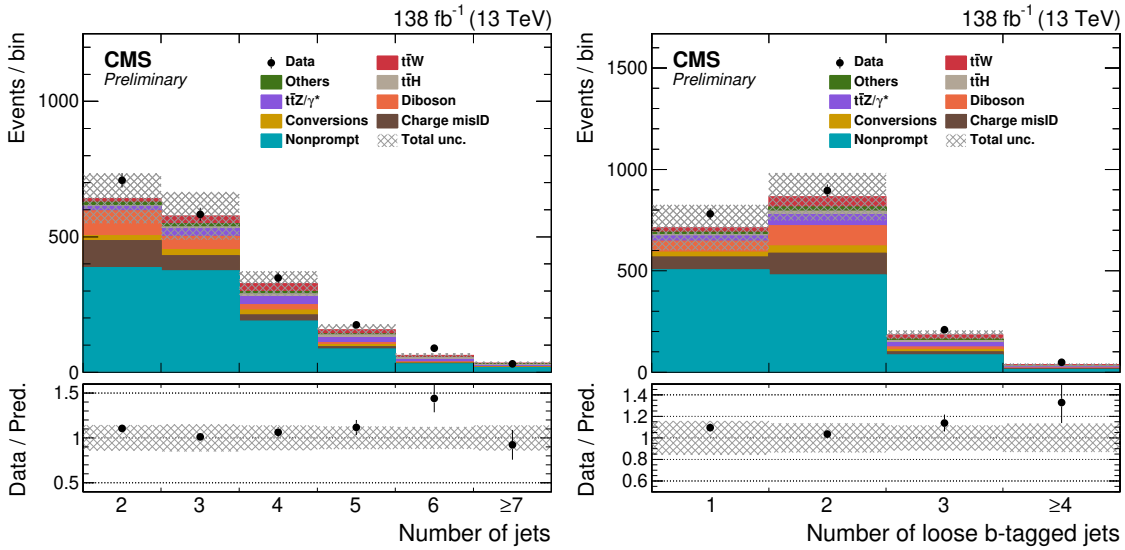

Figure 4: Expected and observed number of events in the validation region enriched in non-prompt leptons. The distributions of the total number of jets (left) and loose b-tagged jets (right) are shown. The lower panel shows the ratio between the number of observed events in data and the total number of predicted events. The error bars represent statistical uncertainty in data, whereas the hatched bands refer to the total systematic uncertainty.

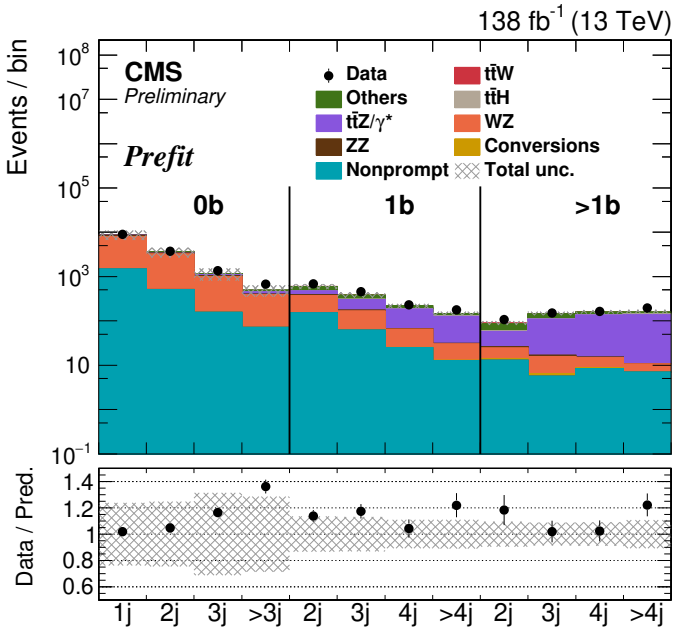

Figure 5: Expected and observed number of events in the control region enriched in WZ and $t\bar{t}Z$ events. Events are categorized by the number of jets (j) and b-tagged jets (b). The lower panel shows the ratio between the number of observed events in data and the total number of predicted events. The error bars represent statistical uncertainty in data, whereas the hatched bands refer to the total systematic uncertainty.

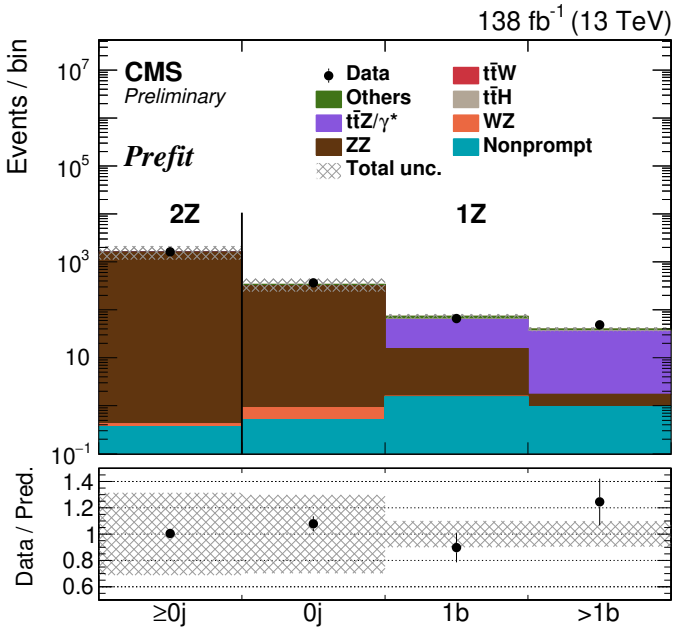

Figure 6: Comparison for the number of selected events in the ZZ control region between data and prediction. Events with two Z boson candidates are included in the first bin, while the other bins contain events with one Z boson candidate and no selected jets, exactly one b-tagged jet, and more than one b-tagged jet. The lower panel shows the ratio between the number of observed events in data and the total number of events expected from the prediction. The error bars show the statistical uncertainty in data, whereas the hatched bands represent the total systematic uncertainty. Small contribution from background processes with nonprompt leptons is estimated using simulation.

each variation. The described uncertainties related to $p_{\mathrm{T}}^{\mathrm{miss}}$ reconstruction are not relevant for the trileptonic channel, where the $p_{\mathrm{T}}^{\mathrm{miss}}$ variable is not used. This systematic uncertainty is considered as partially correlated by data-taking year.

b tagging The uncertainty on the b tagging efficiency scale factors is considered as fully correlated between b and c quark jets, and uncorrelated for other quark flavors. These sources are considered as partially correlated by data-taking year.

Theoretical modelling uncertainties Uncertainties in the modelling of the signal and background processes may impact the acceptance and the extracted cross section in the measurement. All modelling uncertainties are considered as correlated among data-taking years.

Uncertainties in the acceptance of simulated events due to missing higher-order diagrams in event generation at matrix-element level are taken into account using the envelope obtained by separately and simultaneously varying the normalization and factorization scales μ_R and μ_F within a factor of two from their nominal values in each bin, and separating their effect on the acceptance from their change of the cross section, which is taken into account separately. This is done for all backgrounds that are estimated from simulation. For the signal process only the effect on the acceptance is taken into account.

For the signal, the effect of uncertainties in the initial- and final-state radiation in the parton shower on the acceptance is taken into account. The uncertainty due to the color-reconnection model is estimated by using simulated samples produced with alternative models [20], and found to be 1%. The effect on the shape of the signal due to the PDF uncertainty is also taken into account. Using the Hessian NNPDF3.1 set, the difference with respect to the central value is computed for each of the 100 PDF variations; and these variations are added in quadrature. Then, the α_s variation is taken into account adding the variation in quadrature.

Background normalization The normalizations of the $\mathrm{t\bar{t}Z}$, WZ and ZZ backgrounds float freely in the fit and are constrained from the control regions described in Section 6. Since WZ and ZZ events containing a large number of b-tagged jets are either due to misidentified light-flavor jets or due to the inclusion of a phase space region that is not well described in simulation, an additional 40% uncertainty is applied to the predicted number of events with two or more b-tagged jets, as well as a 10% uncertainty for events with fewer than two b-tagged jets, following the studies in Ref. [48]. An additional uncertainty of 30% is applied to WZ and ZZ events with at least three selected jets in order to account for mismodelling effects observed in the trileptonic control region described in Section 6. The normalization of the $\mathrm{t\bar{t}H}$ background is constrained within a 20% uncertainty [8]. The normalization of the $\mathrm{t\bar{t}}\gamma$ process includes an uncertainty of 8% [52]. In order to account for a possible mismodelling of photon conversions in the simulation, an additional 30% uncertainty is applied to the predicted number of events, following the studies performed in Ref. [53]. The normalizations of the tHq and tHW backgrounds are each constrained within a 50% uncertainty. The tZq normalization uncertainty amounts to 10%, following the latest measurement done by CMS [42]. A 50% uncertainty is applied on the $\mathrm{t\bar{t}VV}$ normalization, which reflects the current experimental uncertainty in Ref. [54]. A 50% uncertainty is applied on the triboson production, as the main contribution to this background comes from the WWW production, studied in Ref. [55]. For other background processes with smaller production cross sections, the yields are constrained within 50%, even if most of these processes have been measured with a higher precision, in order to conservatively account for the extrapolation of these predictions to the kinematic region used in the present study, which contains events with high jet and b-tagged jet multiplicities. An uncertainty for the charge misreconstruction probability is derived from the validation of the predicted misreconstruction rates in an orthogonal kinematic region in data, as described in Section 6, and

found to be 20%; since this background is negligible for the trileptonic channel, the uncertainty is not present there.

Nonprompt lepton background The misidentification rates used to estimate the nonprompt lepton background are affected by a statistical uncertainty from the QCD multijet measurement region and inaccuracies in the modelling of the contamination due to prompt leptons in this measurement region. Three systematic uncertanties are introduced, for each lepton flavor, in the prediction of background processes with nonprompt leptons. The first uncertainty modifies the overall normalization of the background prediction. The other two uncertainties incorporate the dependence on the lepton p_{T} and η. These are taken as correlated among the data-taking years. An additional systematic uncertainty of 20% is applied to nonprompt background estimate to cover for discrepancies between the prediction and the observation in the validation region enriched in nonprompt leptons. This systematic uncertainty is taken as correlated among the data-taking years and considered final states.

8 Results

A binned profile likelihood fit is performed to data using the obtained distributions for signal and background processes [56, 57]. The fit is based on the likelihood function that is built from the Poisson probabilities to obtain the observed yields given the predicted signal and background estimates, including their systematic uncertainties and correlations. In the dileptonic channel, the NN output score in eight categories defined by lepton flavor and charge in the dileptonic channel is used. The $m(3\ell)$ distributions are fitted in the trileptonic channel using event categories defined by the b-tagged jet and jet multiplicities, as well as the charges of the leptons. The fit includes event yields, split by lepton flavours, in the b-tagged jet and jet multiplicity bins in the control region enriched in WZ and $\mathrm{t\bar{t}Z}$ events. Event yields in the ZZ control region, split by lepton flavors, are also included in the fit. In addition, each of the described event categories is further split into different data-taking years.

Systematic uncertainties that affect the normalization and not the shape of a predicted distribution are represented in the likelihood fit by a log-normal probability density function. Systematic uncertainties that affect the shape of the discriminating observables are assumed to be Gaussian distributed. Statistical fluctuations in the yields are taken into account through a single nuisance parameter in all processes [58].

A comparison between the total number of observed and predicted events obtained before the fit in the dileptonic and the trileptonic channels is presented in Table 1. Ratios between predicted number of events obtained after the fit to the corresponding number of events before the fit is performed for the signal and the background processes are also shown.

The distributions of the NN output classifiers in the dileptonic channel are presented in Fig. 7. The different shapes of distributions in the final states with positive and negative charges of leptons are due to the fact that the lepton charges are used in NN training as input variables. Figures 8 and 9 show the $m(3\ell)$ distributions obtained in the trileptonic channel, presented in event categories with two or three selected jets, and additional two b-tagged jets.

The effect of various systematic uncertainties that are relevant to the presented study is described in Table 2. The dominant experimental uncertainties include the uncertainties in the integrated luminosity determination, background estimation of electron charge misidentification and b jet identification. Normalization uncertainties in the predictions of the $\mathrm{t\bar{t}H}$, VVV and $\mathrm{t\bar{t}VV}$ processes also represent dominant contributions to the total uncertainty in the measure-

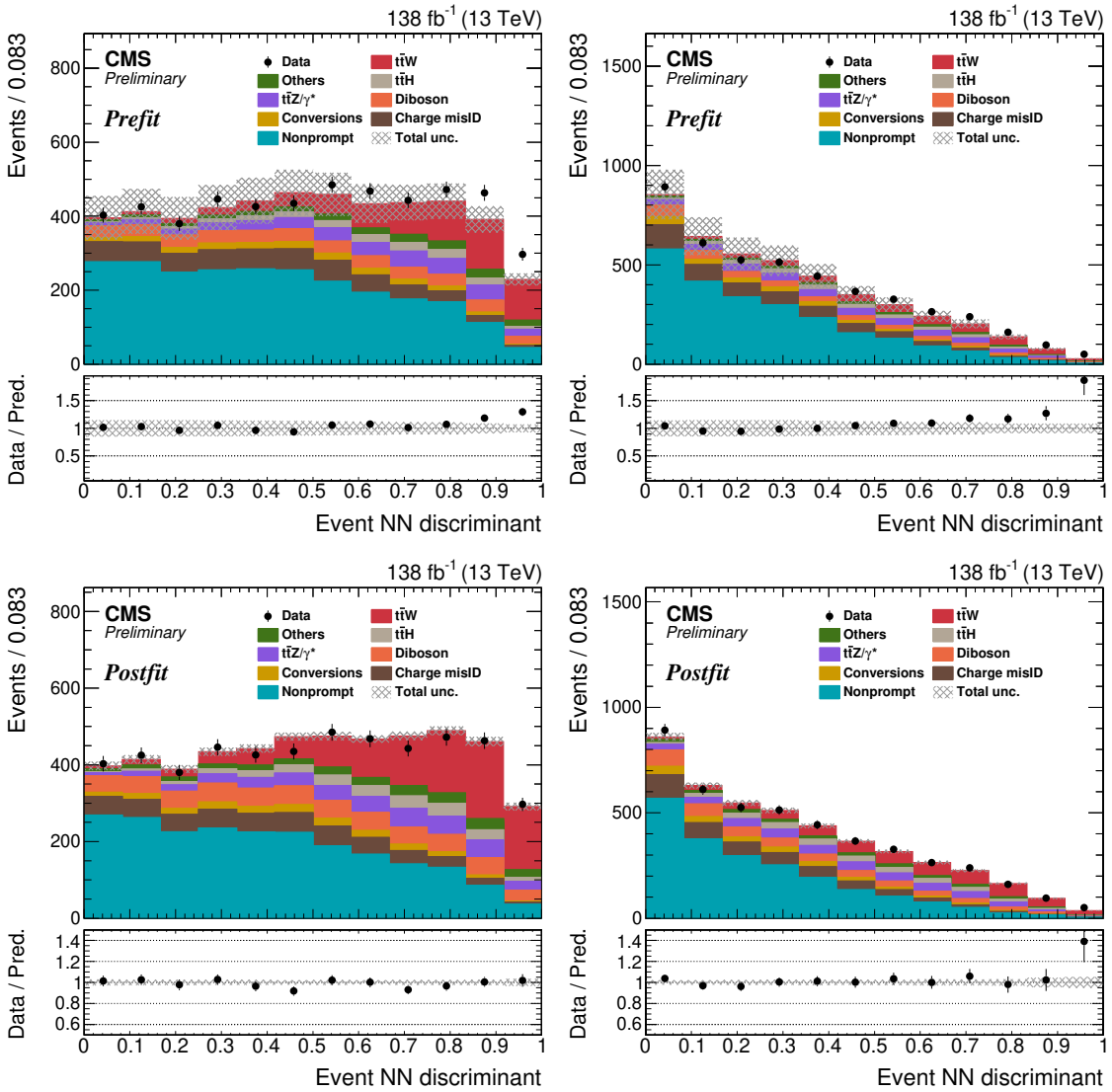

Figure 7: Comparison between observed and predicted events for the NN output score distributions in final states with two leptons of positive (left) and negative (right) charges. The results are shown before (top) and after (bottom) the fit. The lower panels show the ratio between the number of observed events in data, and the total number of predicted events. The error bars show the statistical uncertainty in data, whereas the hatched bands represent the total systematic uncertainty.

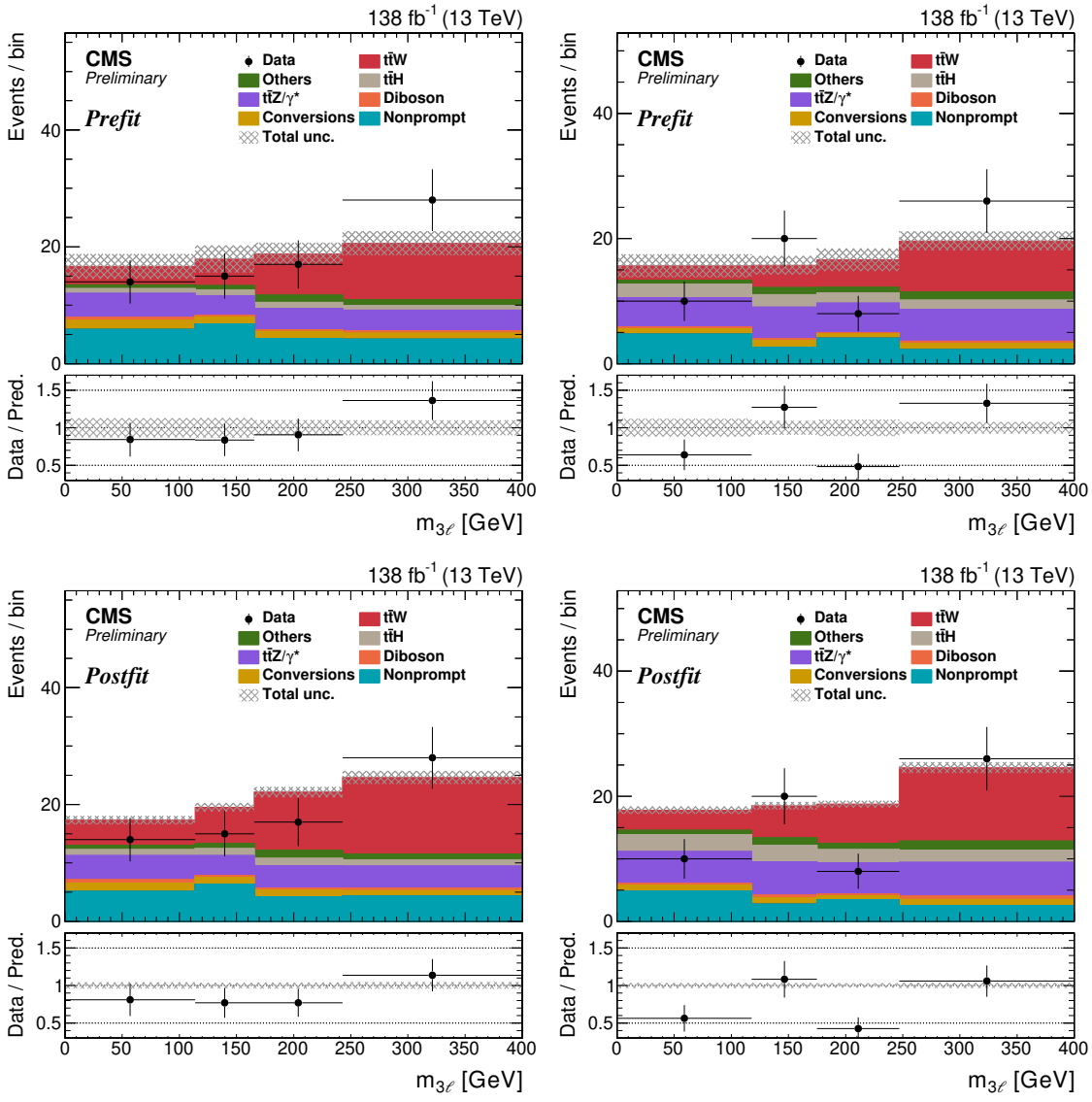

Figure 8: Distributions of the invariant mass of three leptons in events with two (left) and three (right) jets, with two additional b-tagged jets for the positive sum of lepton charges. The results are shown before (top) and after (bottom) the fit. The last bins include the overflows.

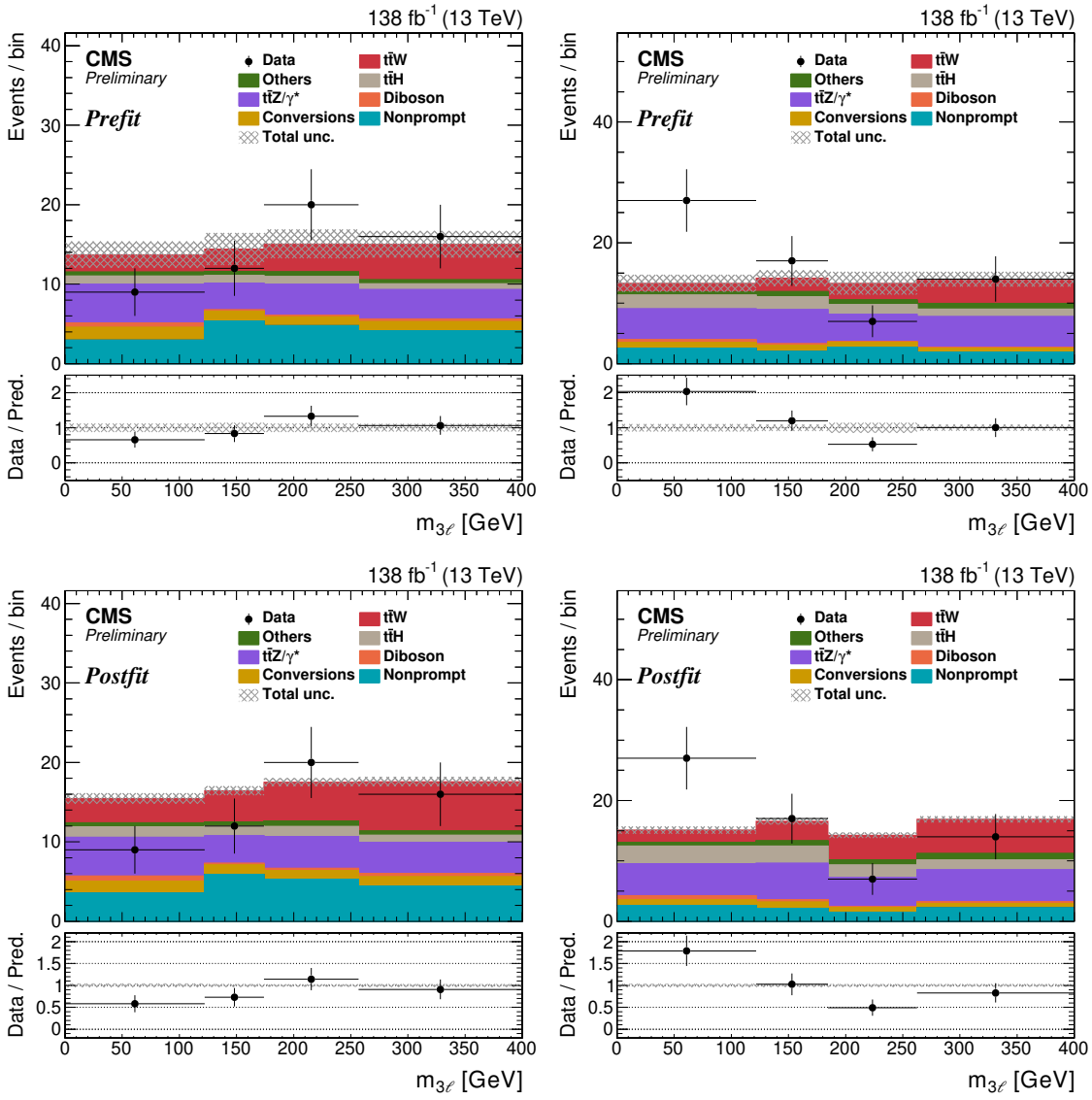

Figure 9: Distributions of the invariant mass of three leptons in events with two (left) and three (right) jets, with two additional b-tagged jets for the negative sum of lepton charges. The results are shown before (top) and after (bottom) the fit. The last bins include the overflows.

ment. Additional important contributions arise from the modelling uncertainties associated with the simulation of $t\bar{t}W$ events and statistical uncertainty in the predicted number of signal and background events.

The precision obtained in the present study is significantly improved with respect to the previous measurement that was performed using a fraction of data collected at $\sqrt{s} = 13\,\text{TeV}$ [5]. This improvement is attributed to a larger data sample, as well as to an improved analysis strategy and improved estimates of dominant background contributions using control regions in data. A larger selection efficiency of $t\bar{t}W$ events and a stronger background suppression are achieved by using the dedicated lepton MVA selection criteria for nonprompt lepton background rejection. Additional improvement in obtained signal-to-background ratio is associated with the enhanced b tagging performance following the installation of the new pixel detector in 2017 and a more performant tagging algorithm [44–46].

In Fig. 10, the measured cross sections for the $t\bar{t}W$ process are compared to the corresponding theoretical predictions. In addition to the theoretical cross section that is used in the present study to normalize the number of predicted $t\bar{t}W$ events [12], the results are also compared to the recent calculation of the $t\bar{t}W$ production cross section using an improved FxFx matrix element merging procedure [16]. The cross sections of the $t\bar{t}W^+$ and the $t\bar{t}W^-$ processes are of special interest because of a strong enhancement of the $t\bar{t}W^+$ production with respect to the $t\bar{t}W^-$ process, due to the valence quark effects in pp collisions. The measurement of the $t\bar{t}W^+$ and the $t\bar{t}W^-$ cross sections therefore provides important information on the PDF of the proton. The cross sections of the $t\bar{t}W^+$ and $t\bar{t}W^-$ processes are measured in a simultaneous fit to data using events categorized by the positive and negative sums of lepton charges. The result of this simultaneous fit is shown in Fig. 11. The measurement of the ratio between the cross sections of the two processes is performed by modifying the fit procedure to directly measure the ratio. The corresponding 68% and 95% confidence level (CL) intervals obtained in the scan of the difference between the negative log-likelihood value and its best fit value are shown in Fig. 12. Measured values of the $t\bar{t}W$, $t\bar{t}W^+$ and $t\bar{t}W^-$ production cross sections, as well as the ratio of the $t\bar{t}W^+$ and $t\bar{t}W^-$ cross sections, $R_{t\bar{t}W^+/t\bar{t}W^-}$, are:

$$\begin{aligned}
\sigma_{t\bar{t}W} &= 868 \pm 40\,(\text{stat})^{+52}_{-50}\,(\text{syst})\,\text{fb} \\
\sigma_{t\bar{t}W^+} &= 553^{+30}_{-29}\,(\text{stat})^{+31}_{-30}\,(\text{syst})\,\text{fb} \\
\sigma_{t\bar{t}W^-} &= 343 \pm 26\,(\text{stat}) \pm 25\,(\text{syst})\,\text{fb} \\
R_{t\bar{t}W^+/t\bar{t}W^-} &= 1.61^{+0.15}_{-0.14}\,(\text{stat})^{+0.07}_{-0.05}\,(\text{syst})
\end{aligned}$$

The measurement of $R_{t\bar{t}W^+/t\bar{t}W^-}$ is associated with reduced relative systematic uncertainty due to partial correlations. The measured cross sections are larger than the corresponding predicted values for the $t\bar{t}W$ [12], $t\bar{t}W^+$ [11] and $t\bar{t}W^-$ [11] processes, while the measured value of $R_{t\bar{t}W^+/t\bar{t}W^-}$ is smaller than its predicted value [11]:

$$\begin{aligned}
\sigma^{\text{theo.}}_{t\bar{t}W} &= 592^{+155}_{-96}(\text{scale})^{+12}_{-12}(\text{PDF})\,\text{fb} \\
\sigma^{\text{theo.}}_{t\bar{t}W^+} &= 384^{+52}_{-32}(\text{scale})^{+8}_{-8}(\text{PDF})\,\text{fb} \\
\sigma^{\text{theo.}}_{t\bar{t}W^-} &= 198^{+26}_{-16}(\text{scale})^{+5}_{-5}(\text{PDF})\,\text{fb} \\
R^{\text{theo.}}_{t\bar{t}W^+/t\bar{t}W^-} &= 1.94^{+0.37}_{-0.24}
\end{aligned}$$

A larger cross section for the $t\bar{t}W$ process is also observed when compared to Ref. [16], in

Table 1: Number of predicted and observed events in the signal regions after the dileptonic and trileptonic selections. The last column shows the ratio between the number of predicted events after and before the fit. The total uncertainty in the number of predicted events is shown. The symbol "—" indicates that the corresponding background does not apply.

Process	$\ell^+\ell^+$	$\ell^-\ell^-$	$\ell^\pm\ell^\mp\ell^+$	$\ell^\pm\ell^\mp\ell^-$	Postfit/Prefit
$t\bar{t}W$	677 ± 21	355 ± 12	119 ± 9	65 ± 5	1.49
Nonprompt	2486 ± 598	2364 ± 570	325 ± 75	298 ± 71	0.91
Charge misID	521 ± 110	523 ± 111	—	—	0.91
$t\bar{t}H$	167 ± 34	169 ± 34	56 ± 12	57 ± 12	1.35
$t\bar{t}Z/\gamma^*$	335 ± 26	333 ± 26	145 ± 13	147 ± 13	1.10
Diboson	382 ± 88	285 ± 65	47 ± 9	38 ± 8	1.07
Others	178 ± 34	126 ± 27	43 ± 8	34 ± 7	1.20
Conversions	177 ± 54	192 ± 59	23 ± 7	24 ± 7	1.01
Total backgrounds	4246 ± 621	3993 ± 591	639 ± 80	597 ± 76	1.03
Total prediction	4922 ± 623	4348 ± 591	758 ± 81	663 ± 76	1.05
Data	5143	4486	834	744	

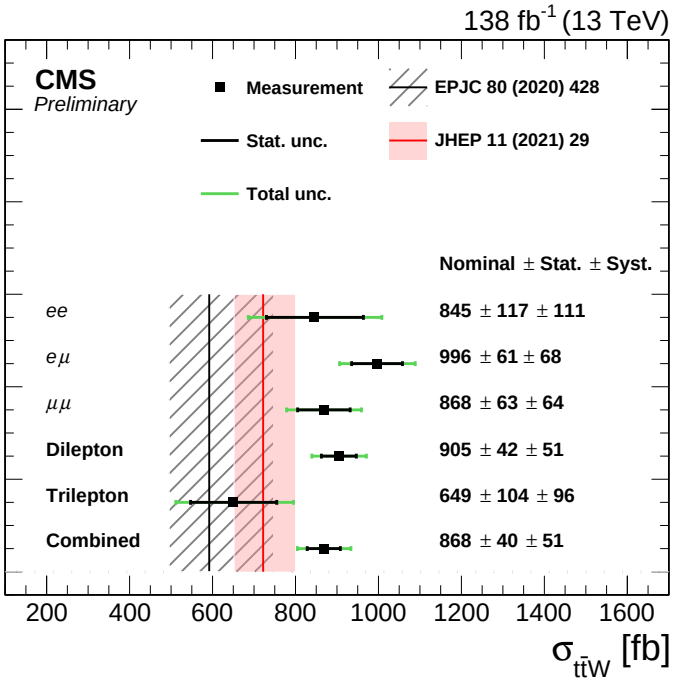

Figure 10: Measured cross sections for the $t\bar{t}W$ production in different final states are compared to theoretical predictions [12, 16]. The cross sections are measured in dilepton (ee, $\mu\mu$, $e\mu$) and trilepton events, as well as in combination of channels.

Uncertainty type	Relative value (%)
Experimental	
Integrated luminosity	1.9
Charge misidentification	1.6
b jet identification	1.6
Nonprompt lepton background	1.3
Trigger efficiencies	1.2
Pileup	1.0
Trigger prefiring	0.7
Jet energy scale	0.6
Jet energy resolution	0.4
Lepton efficiencies	0.4
Normalizations	
$t\bar{t}H$	2.6
VVV	1.2
$t\bar{t}VV$	1.2
Conversions	0.7
$t\bar{t}\gamma$	0.6
ZZ	0.6
Others	0.5
$t\bar{t}Z$	0.3
WZ	0.2
tZq	0.2
tHq	0.2
Modelling	
$t\bar{t}W$ scale	1.8
$t\bar{t}W$ colour reconnection	1.0
ISR/FSR for $t\bar{t}W$	0.8
$t\bar{t}\gamma$ scale	0.4
VVV scale	0.3
$t\bar{t}H$ scale	0.2
Conversions	0.2
Statistical uncertainty	1.8

Table 2: Uncertainties in predicted signal and background events and their impacts on the measured cross section of the $t\bar{t}W$ process. Relative variations of uncertainties are shown when fixing the nuisance parameters associated with that uncertainty in the fit. Systematic uncertainties with an impact larger than 0.1% are shown. Production cross sections of the $t\bar{t}W$, WZ, ZZ and $t\bar{t}Z$ processes are simultaneously constrained in the fit.

agreement with SM predictions within two standard deviations. The $\mathrm{t\bar{t}W}$ production cross section and the $R_{\mathrm{t\bar{t}W^+/t\bar{t}W^-}}$ value are measured with the total uncertainties that are a factor of two smaller than the corresponding uncertainties associated with theoretical predictions [11, 12, 16]. The measured $R_{\mathrm{t\bar{t}W^+/t\bar{t}W^-}}$ value is found to be in agreement with the SM predictions.

9 Summary

The cross section for the associated production of a W boson with a pair of top quarks ($\mathrm{t\bar{t}W}$) in proton-proton collisions at a center-of-mass energy of 13 TeV is measured using 138 fb^{-1} of data collected by the CMS detector. The measurement is performed in final states with two or three leptons. The measured cross section is $868 \pm 40\,(\mathrm{stat})^{+52}_{-50}\,(\mathrm{syst})$ fb. The cross sections for the associated production of a top quark pair with a W^+ and a W^- boson are $553^{+30}_{-29}\,(\mathrm{stat})^{+31}_{-30}\,(\mathrm{syst})$ fb and $343 \pm 26\,(\mathrm{stat}) \pm 25\,(\mathrm{syst})$ fb, respectively. The measured ratio between these production cross sections is $1.61^{+0.15}_{-0.14}\,(\mathrm{stat})^{+0.07}_{-0.05}\,(\mathrm{syst})$. The obtained results are in agreement with standard model predictions within two standard deviations.

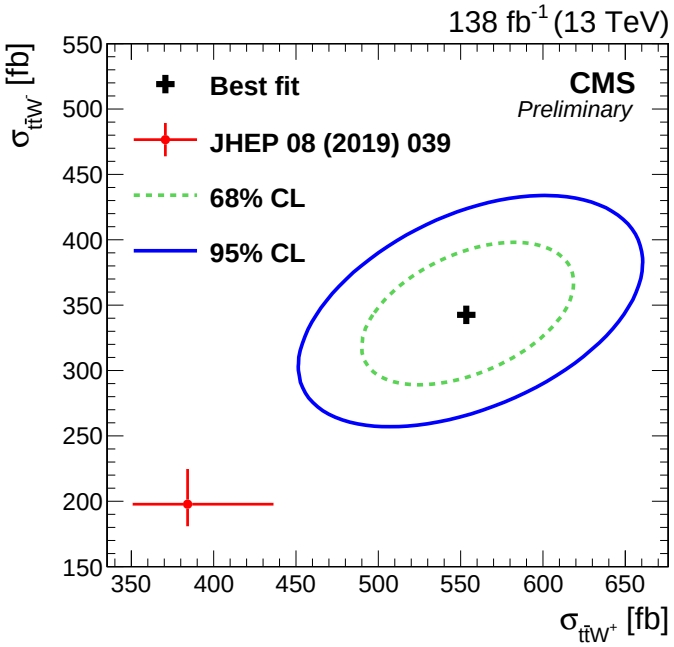

Figure 11: The 68% and 95% CL intervals in the likelihood fit with the $t\bar{t}W^+$ and $t\bar{t}W^-$ cross sections measured independently. The intervals are shown as contours. The best fit value is indicated by the black cross, while the predicted value [11] is shown as the red circle. The prediction that is used in the presented comparison does not include the improved FxFx matrix element merging procedure, which is described in Ref. [16].

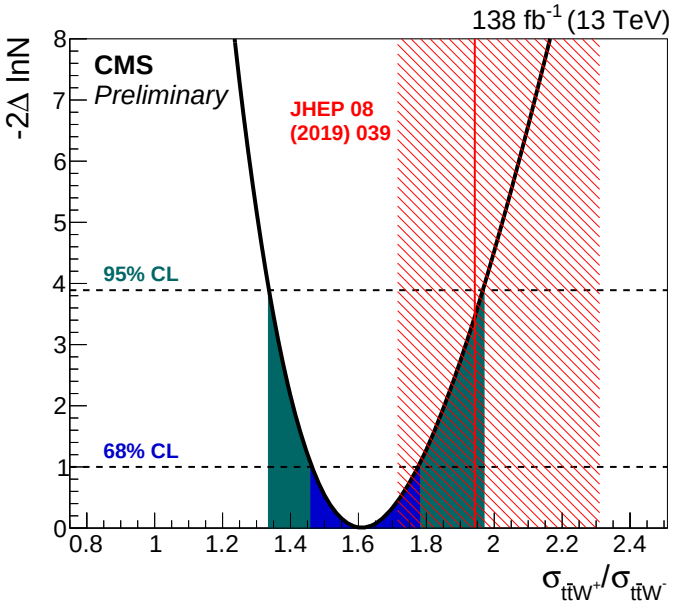

Figure 12: Distributions of the negative log-likelihood value difference from the best fit value for the scan of the ratio of the $t\bar{t}W^+$ and $t\bar{t}W^-$ cross sections. The blue (green) bands indicate the 68% and 95% CL limits on the ratio of the cross sections. The SM prediction (red line) and its uncertainty (red band) are taken from Ref. [11].

References

[1] O. Bessidskaia Bylund et al., "Probing top quark neutral couplings in the Standard Model Effective Field Theory at NLO QCD", *JHEP* **05** (2016) 052, doi:10.1007/JHEP05(2016)052, arXiv:1601.08193.

[2] J. A. Dror, M. Farina, E. Salvioni, and J. Serra, "Strong tW Scattering at the LHC", *JHEP* **01** (2016) 071, doi:10.1007/JHEP01(2016)071, arXiv:1511.03674.

[3] A. Buckley et al., "Constraining top quark effective theory in the LHC Run II era", *JHEP* **04** (2016) 015, doi:10.1007/JHEP04(2016)015, arXiv:1512.03360.

[4] F. Maltoni, M. L. Mangano, I. Tsinikos, and M. Zaro, "Top-quark charge asymmetry and polarization in $t\bar{t}W^{\pm}$ production at the LHC", *Phys. Lett. B* **736** (2014) 252, doi:10.1016/j.physletb.2014.07.033, arXiv:1406.3262.

[5] CMS Collaboration, "Measurement of the cross section for top quark pair production in association with a W or Z boson in proton-proton collisions at $\sqrt{s} = 13$ TeV", *JHEP* **08** (2018) 011, doi:10.1007/JHEP08(2018)011, arXiv:1711.02547.

[6] ATLAS Collaboration, "Measurement of the $t\bar{t}Z$ and $t\bar{t}W$ cross sections in proton-proton collisions at $\sqrt{s} = 13$ TeV with the ATLAS detector", *Phys. Rev. D* **99** (2019) 072009, doi:10.1103/PhysRevD.99.072009, arXiv:1901.03584.

[7] ATLAS Collaboration, "Analysis of $t\bar{t}H$ and $t\bar{t}W$ production in multilepton final states with the ATLAS detector", ATLAS Conference Note ATLAS-CONF-2019-045, 2019.

[8] CMS Collaboration, "Measurement of the Higgs boson production rate in association with top quarks in final states with electrons, muons, and hadronically decaying tau leptons at $\sqrt{s} = 13$ TeV", *Eur. Phys. J. C* **81** (2021) 378, doi:10.1140/epjc/s10052-021-09014-x, arXiv:2011.03652.

[9] CMS Collaboration, "Search for production of four top quarks in final states with same-sign or multiple leptons in proton-proton collisions at $\sqrt{s} = 13$ TeV", *Eur. Phys. J. C* **80** (2020) 75, doi:10.1140/epjc/s10052-019-7593-7, arXiv:1908.06463.

[10] ATLAS Collaboration, "Evidence for $t\bar{t}t\bar{t}$ production in the multilepton final state in proton–proton collisions at $\sqrt{s} = 13$ TeV with the ATLAS detector", *Eur. Phys. J. C* **80** (2020) 1085, doi:10.1140/epjc/s10052-020-08509-3, arXiv:2007.14858.

[11] A. Broggio et al., "Top-quark pair hadroproduction in association with a heavy boson at NLO+NNLL including EW corrections", *JHEP* **08** (2019) 039, doi:10.1007/JHEP08(2019)039, arXiv:1907.04343.

[12] A. Kulesza et al., "Associated top quark pair production with a heavy boson: differential cross sections at NLO+NNLL accuracy", *Eur. Phys. J. C* **80** (2020) 428, doi:10.1140/epjc/s10052-020-7987-6, arXiv:2001.03031.

[13] G. Bevilacqua et al., "NLO QCD corrections to off-shell $t\bar{t}W^{\pm}$ production at the LHC: Correlations and Asymmetries", *Eur. Phys. J. C* **81** (2021) 675, doi:10.1140/epjc/s10052-021-09478-x, arXiv:2012.01363.

[14] S. von Buddenbrock, R. Ruiz, and B. Mellado, "Anatomy of inclusive $t\bar{t}W$ production at hadron colliders", *Phys. Lett. B* **811** (2020) 135964, doi:10.1016/j.physletb.2020.135964, arXiv:2009.00032.

[15] R. Frederix and I. Tsinikos, "Subleading EW corrections and spin-correlation effects in $t\bar{t}W$ multi-lepton signatures", *Eur. Phys. J. C* **80** (2020) 803, doi:10.1140/epjc/s10052-020-8388-6, arXiv:2004.09552.

[16] R. Frederix and I. Tsinikos, "On improving NLO merging for $t\bar{t}W$ production", *JHEP* **11** (2021) 29, doi:10.1007/JHEP11(2021)029, arXiv:2108.07826.

[17] CMS Collaboration, "The CMS trigger system", *JINST* **12** (2017) P01020, doi:10.1088/1748-0221/12/01/P01020, arXiv:1609.02366.

[18] J. Alwall et al., "The automated computation of tree-level and next-to-leading order differential cross sections, and their matching to parton shower simulations", *JHEP* **07** (2014) 079, doi:10.1007/JHEP07(2014)079, arXiv:1405.0301.

[19] G. Bevilacqua et al., "The simplest of them all: $t\bar{t}W^{\pm}$ at NLO accuracy in QCD", *JHEP* **08** (2020) 043, doi:10.1007/JHEP08(2020)043, arXiv:2005.09427.

[20] CMS Collaboration, "A new set of CMS tunes for novel colour reconnection models in PYTHIA8 based on underlying-event data", CMS Physics Analysis Summary CMS-PAS-GEN-17-002, 2021.

[21] P. Nason, "A new method for combining NLO QCD with shower Monte Carlo algorithms", *JHEP* **11** (2004) 040, doi:10.1088/1126-6708/2004/11/040, arXiv:hep-ph/0409146.

[22] S. Frixione, P. Nason, and C. Oleari, "Matching NLO QCD computations with parton shower simulations: the POWHEG method", *JHEP* **11** (2007) 070, doi:10.1088/1126-6708/2007/11/070, arXiv:0709.2092.

[23] S. Alioli, P. Nason, C. Oleari, and E. Re, "A general framework for implementing NLO calculations in shower Monte Carlo programs: the POWHEG BOX", *JHEP* **06** (2010) 043, doi:10.1007/JHEP06(2010)043, arXiv:1002.2581.

[24] T. Sjöstrand et al., "An introduction to PYTHIA 8.2", *Comput. Phys. Commun.* **191** (2015) 159, doi:10.1016/j.cpc.2015.01.024, arXiv:1410.3012.

[25] P. Skands, S. Carrazza, and J. Rojo, "Tuning PYTHIA 8.1: the Monash 2013 tune", *Eur. Phys. J. C* **74** (2014) 3024, doi:10.1140/epjc/s10052-014-3024-y, arXiv:1404.5630.

[26] CMS Collaboration, "Extraction and validation of a new set of CMS PYTHIA8 tunes from underlying-event measurements", *Eur. Phys. J. C* **80** (2020) doi:10.1140/epjc/s10052-019-7499-4, arXiv:1903.12179.

[27] CMS Collaboration, "Event generator tunes obtained from underlying event and multiparton scattering measurements", *Eur. Phys. J. C* **76** (2016) 155, doi:10.1140/epjc/s10052-016-3988-x, arXiv:1512.00815.

[28] CMS Collaboration, "Investigations of the impact of the parton shower tuning in Pythia 8 in the modelling of $t\bar{t}$ at $\sqrt{s} = 8$ and 13 TeV", CMS Physics Analysis Summary CMS-PAS-TOP-16-021, 2016.

[29] R. Frederix and S. Frixione, "Merging meets matching in MC@NLO", *JHEP* **12** (2012) 61, doi:10.1007/JHEP12(2012), arXiv:1209.6215.

[30] NNPDF Collaboration, "Parton distributions from high-precision collider data", *Eur. Phys. J. C* **77** (2017) 663, doi:10.1140/epjc/s10052-017-5199-5, arXiv:1706.00428.

[31] GEANT4 Collaboration, "GEANT4—a simulation toolkit", *Nucl. Instrum. Meth. A* **506** (2003) 250, doi:10.1016/S0168-9002(03)01368-8.

[32] CMS Collaboration, "Particle-flow reconstruction and global event description with the CMS detector", *JINST* **12** (2017) P10003, doi:10.1088/1748-0221/12/10/P10003, arXiv:1706.04965.

[33] CMS Collaboration, "Performance of reconstruction and identification of τ leptons decaying to hadrons and ν_τ in pp collisions at $\sqrt{s} = 13$ TeV", *JINST* **13** (2018), no. 10, P10005, doi:10.1088/1748-0221/13/10/P10005, arXiv:1809.02816.

[34] CMS Collaboration, "Jet energy scale and resolution in the CMS experiment in pp collisions at 8 TeV", *JINST* **12** (2017) P02014, doi:10.1088/1748-0221/12/02/P02014, arXiv:1607.03663.

[35] CMS Collaboration, "Performance of missing transverse momentum reconstruction in proton-proton collisions at $\sqrt{s} = 13$ TeV using the CMS detector", *JINST* **14** (2019) P07004, doi:10.1088/1748-0221/14/07/P07004, arXiv:1903.06078.

[36] M. Cacciari, G. P. Salam, and G. Soyez, "The anti-k_T jet clustering algorithm", *JHEP* **04** (2008) 063, doi:10.1088/1126-6708/2008/04/063, arXiv:0802.1189.

[37] M. Cacciari, G. P. Salam, and G. Soyez, "FastJet User Manual", *Eur. Phys. J. C* **72** (2012) 1896, doi:10.1140/epjc/s10052-012-1896-2, arXiv:1111.6097.

[38] CMS Collaboration, "Performance of electron reconstruction and selection with the CMS detector in proton-proton collisions at $\sqrt{s} = 8$ TeV", *JINST* **10** (2015) P06005, doi:10.1088/1748-0221/10/06/P06005, arXiv:1502.02701.

[39] CMS Collaboration, "Performance of the CMS muon detector and muon reconstruction with proton-proton collisions at $\sqrt{s} = 13$ TeV", *JINST* **13** (2018) P06015, doi:10.1088/1748-0221/13/06/P06015, arXiv:1804.04528.

[40] CMS Collaboration, "Search for new physics in same-sign dilepton events in proton-proton collisions at $\sqrt{s} = 13$ TeV", *Eur. Phys. J. C* **76** (2016) 8, doi:10.1140/epjc/s10052-016-4261-z, arXiv:1605.03171.

[41] CMS Collaboration, "Observation of single top quark production in association with a Z boson in proton-proton collisions at $\sqrt{s} = 13$ TeV", *Phys. Rev. Lett.* **122** (2019) 132003, doi:10.1103/PhysRevLett.122.132003, arXiv:1812.05900.

[42] CMS Collaboration, "Inclusive and differential cross section measurements of single top quark production in association with a Z boson in proton-proton collisions at $\sqrt{s} = 13$ TeV", *JHEP* **02** (2022) 107, doi:10.1007/JHEP02(2022)107, arXiv:2111.02860.

[43] CMS Collaboration, "Pileup mitigation at cms in 13 tev data", *JINST* **15** (2020) P09018, doi:10.1088/1748-0221/15/09/P09018, arXiv:2003.00503.

[44] CMS Collaboration, "Identification of heavy-flavour jets with the CMS detector in pp collisions at 13 TeV", *JINST* **13** (2018) P05011, doi:10.1088/1748-0221/13/05/P05011, arXiv:1712.07158.

[45] E. Bols et al., "Jet Flavour Classification Using DeepJet", *JINST* **15** (2020) P12012, doi:10.1088/1748-0221/15/12/P12012, arXiv:2008.10519.

[46] CMS Collaboration, "Performance of the DeepJet b tagging algorithm using 41.9 fb^{-1} of data from proton-proton collisions at 13 TeV with Phase 1 CMS detector", CMS Detector Performance Note CMS-DP-2018-058, 2018.

[47] Particle Data Group, P. A. Zyla et al., "Review of particle physics", *Prog. Theor. Exp. Phys.* **2020** (2020) 083C01, doi:10.1093/ptep/ptaa104.

[48] CMS Collaboration, "Evidence for associated production of a Higgs boson with a top quark pair in final states with electrons, muons, and hadronically decaying τ leptons at $\sqrt{s} = 13$ TeV", *JHEP* **08** (2018) 066, doi:10.1007/JHEP08(2018)066, arXiv:1803.05485.

[49] CMS Collaboration, "Precision luminosity measurement in proton-proton collisions at $\sqrt{s} = 13$ TeV in 2015 and 2016 at CMS", *Eur. Phys. J. C* **81** (2021) 800, doi:10.1140/epjc/s10052-021-09538-2, arXiv:2104.01927.

[50] CMS Collaboration, "CMS luminosity measurement for the 2017 data-taking period at $\sqrt{s} = 13$ TeV", CMS Physics Analysis Summary CMS-PAS-LUM-17-004, 2018.

[51] CMS Collaboration, "CMS luminosity measurement for the 2018 data-taking period at $\sqrt{s} = 13$ TeV", CMS Physics Analysis Summary CMS-PAS-LUM-18-002, 2019.

[52] CMS Collaboration, "Measurement of the inclusive and differential $t\bar{t}\gamma$ cross sections in the single-lepton channel and EFT interpretation at $\sqrt{s} = 13$ TeV", *JHEP* **12** (2021) 80, doi:10.1007/JHEP12(2021)180, arXiv:2107.01508.

[53] CMS Collaboration, "Search for electroweak production of charginos and neutralinos in multilepton final states in proton-proton collisions at $\sqrt{s} = 13$ TeV", *JHEP* **03** (2018) 166, doi:10.1007/JHEP03(2018)166, arXiv:1709.05406.

[54] CMS Collaboration, "Search for standard model production of four top quarks with same-sign and multilepton final states in proton–proton collisions at $\sqrt{s} = 13$ TeV", *Eur. Phys. J. C* **78** (2018) 140, doi:10.1140/epjc/s10052-018-5607-5, arXiv:1710.10614.

[55] CMS Collaboration, "Observation of the Production of Three Massive Gauge Bosons at $\sqrt{s}$ =13 TeV", *Phys. Rev. Lett.* **125** (2020) 151802, doi:10.1103/PhysRevLett.125.151802, arXiv:2006.11191.

[56] ATLAS Collaboration, CMS Collaboration, and LHC Higgs Combination Group, "Procedure for the LHC Higgs boson search combination in Summer 2011", Technical Report CMS-NOTE-2011-005, ATL-PHYS-PUB-2011-011, 2011.

[57] G. Cowan, K. Cranmer, E. Gross, and O. Vitells, "Asymptotic formulae for likelihood-based tests of new physics", *Eur. Phys. J. C* **71** (2011) 1554, doi:10.1140/epjc/s10052-011-1554-0, arXiv:1007.1727. [Erratum: doi:10.1140/epjc/s10052-013-2501-z].

[58] R. J. Barlow and C. Beeston, "Fitting using finite Monte Carlo samples", *Comput. Phys. Commun.* **77** (1993) 219, doi:10.1016/0010-4655(93)90005-W.